







Role of disorder in the synthesis of metastable zinc zirconium nitrides

Rachel Woods-Robinson ^{1,2,3,*} Vladan Stevanović,^{4,3} Stephan Lany ³ Karen N. Heinselman ³
Matthew K. Horton ² Kristin A. Persson ^{5,6} and Andriy Zakutayev ^{3,†}

¹Applied Science and Technology Graduate Group,

University of California at Berkeley, Berkeley, California 94720, USA

²Materials Sciences Division, Lawrence Berkeley National Laboratory, Berkeley, California 94720, USA

³Materials Science Center, National Renewable Energy Laboratory, Golden, Colorado 80401, USA

⁴Department of Metallurgical and Materials Engineering, Colorado School of Mines, Golden, Colorado 80401, USA

⁵Department of Materials Science and Engineering, University of California at Berkeley, Berkeley, California 94720, USA

⁶Molecular Foundry, Lawrence Berkeley National Laboratory, Berkeley, California 94720, USA



(Received 30 August 2021; revised 16 November 2021; accepted 11 March 2022; published 21 April 2022)

In materials science, it is often assumed that ground-state crystal structures predicted by density functional theory are the easiest polymorphs to synthesize. Ternary nitride materials, with many possible metastable polymorphs, provide a rich materials space to study what influences thermodynamic stability and polymorph synthesizability. For example, ZnZrN_2 is theoretically predicted at zero Kelvin to have an unusual layered “wurtsalt” ground-state crystal structure with compelling optoelectronic properties, but it is unknown whether this structure can be realized experimentally under practical synthesis conditions. Here, we use combinatorial sputtering to synthesize hundreds of $\text{Zn}_x\text{Zr}_{1-x}\text{N}_y$ thin-film samples, and find metastable rocksalt-derived or boron-nitride-derived structures rather than the predicted wurtsalt structure. Using a statistical polymorph sampler approach, it is demonstrated that although rocksalt is the least stable polymorph at zero Kelvin, it becomes the most stable polymorph at high effective temperatures similar to those achieved using this sputter deposition method, and thus corroborates experimental results. Additional calculations show that this destabilization of the wurtsalt polymorph is due to configurational entropic and enthalpic effects, and that vibrational contributions are negligible. Specifically, rocksalt- and boron-nitride-derived structures become the most stable polymorphs in the presence of disorder because of higher tolerances to cation cross substitution and off stoichiometry than the wurtsalt structure. This understanding of the role of disorder tolerance in the synthesis of competing polymorphs can enable more accurate predictions of synthesizable crystal structures and their achievable material properties.

DOI: [10.1103/PhysRevMaterials.6.043804](https://doi.org/10.1103/PhysRevMaterials.6.043804)

I. INTRODUCTION

Computational materials discovery is a rapidly progressing research field, with the potential to revolutionize how materials are designed and developed. However, determining whether a given predicted crystalline material is *actually experimentally synthesizable* remains a key challenge. One common assumption in computational materials research is that the ground-state structure predicted by density functional theory (DFT) within the zero-Kelvin (0-K) approximation, or structures with energies near the ground-state energy, are the most likely to be experimentally realized. Conversely, another assumption is that increased energetic instability (i.e.,

formation energy farther away from the ground-state energy) correlates with an increased difficulty to synthesize. However, neither of these assumptions necessarily hold, as demonstrated by multiple experimental and computational studies [1]. Recent work has emerged to further explore synthesizability in metastable materials [2–5], but so far computational materials researchers still cannot confidently answer the following question: “Can this predicted material be synthesized?” [6]. Thus, as materials databases grow and structure predictions yield new predicted compounds for high-throughput screenings, it is increasingly pertinent that the computational materials discovery community develops comprehensive methods for assessing synthesizability so that misleading false positives and negatives can be avoided.

Nitrides provide a compelling class of materials through which to examine synthesizability, in part because they are more likely than any other anion class to crystallize in metastable phases [3,4,7,8]. Recent computational predictions have yielded a multitude of new ternary nitride materials to explore [9,10], yet an understanding of which polymorphs are experimentally synthesizable remains elusive. The chemical and structural richness of this emerging class of materials, including their mixed ionic-covalent nature compared to oxides, provides new candidates for various applications such as hydrogen storage, photovoltaic (PV)

*rwoodsrobinson@lbl.gov

†Andriy.Zakutayev@nrel.gov

Published by the American Physical Society under the terms of the [Creative Commons Attribution 4.0 International](https://creativecommons.org/licenses/by/4.0/) license. Further distribution of this work must maintain attribution to the author(s) and the published article’s title, journal citation, and DOI. Open access publication funded by the National Renewable Energy Laboratory (NREL) Library, part of a national laboratory of the U.S. Department of Energy.

devices, and light-emitting diodes (LEDs). One such emerging class of ternary nitrides is the II-IV-N₂ family, ternary analogs of GaN and promising candidates for PV absorbers and green LEDs. II-IV-N₂ materials are commonly studied in two prototype classes: (1) wurtzite-derived (WZ) structures, with fourfold-coordinated cations (e.g., Zn-based ZnSnN₂, ZnGeN₂, ZnSnP₂, ZnSiP₂) [11] and (2) rocksalt-derived structures (RS), with sixfold-coordinated cations (e.g., MgTMN₂) [12]. Some compounds (e.g., MgSnN₂) have been shown to cocrystallize in both of these configurations at certain growth conditions, such as at ambient temperature at Mg-rich stoichiometries or at increased synthesis temperature on GaN substrates [13,14]. However, these two structure classes are just a small subset of possible structure classes in the rich space of ternary nitrides; it remains unknown which other II-IV-N₂ polymorph structures and chemistries are stabilizable.

Of particular interest to this study is the experimentally empty region of phase space in the zinc-zirconium-nitride (Zn-Zr-N) material system, in particular at its II-IV-N₂ composition ZnZrN₂, which serves as a case study to gain insight for ternary nitrides as a whole. In contrast to other II-IV-N₂ materials, ZnZrN₂ (as well as isoelectronic ZnHfN₂) has a DFT-predicted *P3m1* (156) space-group ground-state structure—a layer of Zn atoms tetrahedrally coordinated by N (wurtzitelike), a layer of Zr atoms octahedrally coordinated by N (rocksaltlike), and alternating Zn and Zr layers—which has been corroborated by three different computational studies using three distinct structure prediction algorithms with DFT relaxations [9,10,15]. This structure is analogous to sulfosalt ScCuS₂, though a corresponding mineral name could not be located [16,17]; thus, we herein refer to this structure type as “wurtsalt” (WS), an amalgam of *wurtzite* and *rocksalt*, and depict the ZnZrN₂ WS structure in the top left of Fig. 1(a), alongside other polymorphs. Despite these predictions, to our knowledge no semiconducting nitride materials in the Zn_xZr_{1-x}N_y ternary space have ever been stabilized experimentally, and it has not yet been investigated whether any other polymorphs exist.

In this study, we demonstrate that certain polymorphs can be preferentially stabilized or destabilized due to their tolerance to disorder. First, a set of 28 possible ZnZrN₂ polymorphs are predicted and investigated computationally. Next, combinatorial sputter synthesis is used to explore the full cation phase space of Zn_xZr_{1-x}N_y heterovalent heterostructural alloys (note that for simplicity, “alloy” will be used herein to represent this system), focusing on the region where $y \approx 1$ and $x \approx 0.5$ close to the ZnZrN₂ stoichiometry. Under this range of experimental sputtering conditions, the cation-ordered WS ground-state structure predicted by DFT at 0 K is *not* synthesized. Instead, a disordered metastable rocksalt (RS) polymorph is synthesized close to the ZnZrN₂ stoichiometry, and a metastable hexagonal boron-nitride-derived (BN) phase is observed at higher Zn concentrations ($x \gtrsim 0.5$). We note that the term “metastable” herein refers to solids that are metastable with respect to computed DFT energies at 0 K, as described in Sun *et al.* [3]. To understand the effects of disorder on the synthesis of ZnZrN₂, a series of computational methods are then applied. We start with the 0-K DFT approximation to reflect how Zn-Zr-N polymorphs would be energetically ranked in computational databases, and then take into account configurational entropy and enthalpy to account

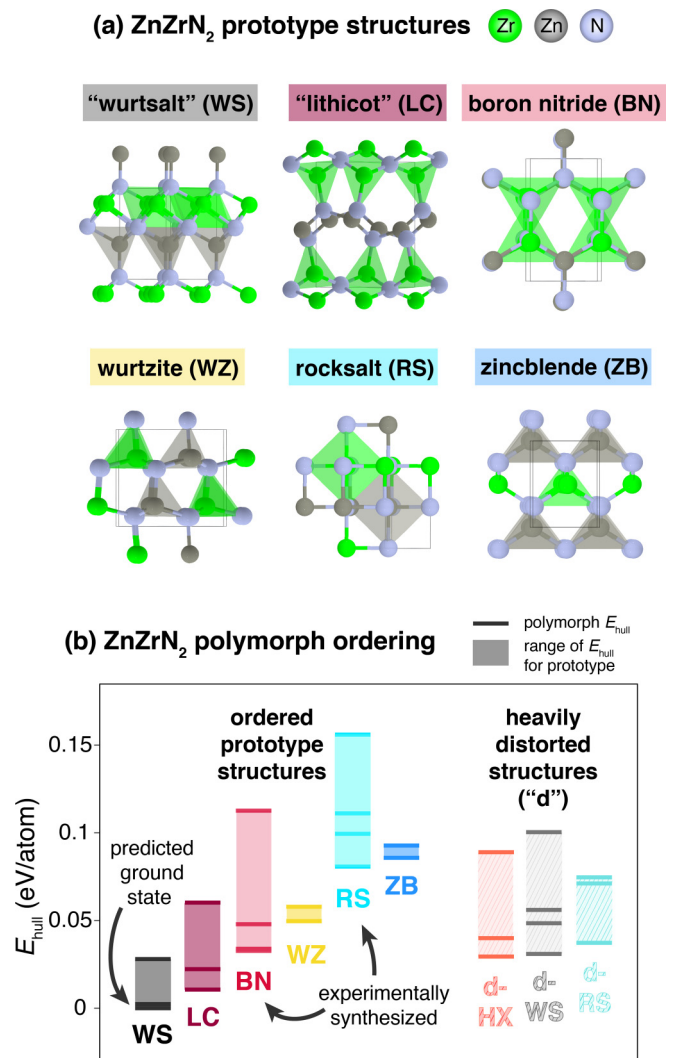


FIG. 1. (a) Representative crystal structures for each of the six ordered structure prototype classes, and (b) energy ordering of the predicted ordered polymorphs, grouped by structure prototype class, with labeled experimentally synthesized phases from this study. Horizontal solid lines in (b) correspond to calculated E_{hull} values of individual polymorphs, and shaded regions correspond to the range of E_{hull} for a given prototype class. Heavily distorted versions of the prototype structures, designated with a “d” prefix, are plotted separately on the right of (b), and “HX” designates distorted hexagonal structures as described in the text.

for temperature, as well as off stoichiometry. These ZnZrN₂ results suggest that it is necessary to consider the effects of disorder tolerance on energetic stabilization in possible polymorphs when investigating other new ternary nitrides, and new computationally predicted materials in general.

II. METHODS

A. Synthesis

Thin-film samples were grown using radio-frequency (RF) cosputter deposition and the combinatorial method, resulting in a total of 24 thin-film combinatorial “libraries” of Zn_xZr_{1-x}N deposited on 50 × 50 mm fused silica substrates

in two different sputter chambers, with various experimental conditions. After exploratory depositions, 11 libraries are reported here, all grown in the same chamber. The chamber setup consists of 2-in. precursor sputter targets of metallic Zr and Zn, with sputter guns pointed towards one another to result in a gradient in cation composition, as depicted in the Supplemental Material (SM) [18]. The samples reported in this study are deposited in an Ar/N₂ environment, with a chamber base pressure of $\sim 2 \times 10^{-7}$ Torr, growth pressure of 5 mTorr, and gas flow rates of Ar and N₂ both of 6 sccm. In an attempt to increase nitrogen chemical potential, a nitrogen cracker is operated during growth at 300 W with 0 W reflected power, measurement tools, with a 4×11 . The rf power is varied from 30–100 W on the gun with the Zn target, and 20–100 W on the gun with the Zr. Temperature gradient methodology and associated temperature calibrations are described elsewhere [19,20] and in the SM [18].

B. Characterization

Material composition and structure was characterized with customized combinatorial measurement tools, with a 4×11 mapping grid projected onto each sample library resulting in 44 data points per library and thus >400 unique compositional data points total in this study. Analysis is conducted using the customized COMBIGOR software package [21]. Film cation composition, i.e., x in Zn _{x} Zr _{$1-x$} N, and film thickness were determined using mapping style x-ray fluorescence (XRF) spectroscopy and Dektak profilometry. Since nitrogen (as well as spurious oxygen) cannot be resolved with XRF, a select number of samples are measured using Rutherford backscattering spectrometry (RBS) to confirm cation composition and to measure the anion content in films. RBS was performed at NREL on a National Electrostatics Corporation 3S-MR10 instrument with a 2-MeV alpha particle beam at a current of 70 nA. The total accumulated charge was 320 μ C, and the RBS detector was mounted in a backscatter configuration at 140°. Analysis was performed with the RUMP package. Structural analysis mapping was performed for all libraries with x-ray diffraction (XRD) on a Bruker D8 Discover with a θ - 2θ geometry, Cu $K\alpha$ radiation, and a proportional two-dimensional (2D) detector. Measurements are complemented for 11 libraries of interest at Beam Line 1-5 at the Stanford Synchrotron Radiation Lightsource (SSRL) with wide-angle x-ray scattering (WAXS). 2D scattering was collected with a Rayonix 165 CCD camera at grazing incidence at an incident energy of 12.7 keV.

C. Polymorph structure generation

Candidate ordered polymorphs were generated using kinetically limited minimization (KLM) [22] and ionic substitution of prototypes from other ternary nitrides [14]. Unique structures that emerged from the polymorph sampler random structure searching were also included as ordered polymorphs [2]. To create a set of ordered prototype “alloys” across the ZrN-ZnN tieline (i.e., Zn _{x} Zr _{$1-x$} N), we performed cation substitution in each of the ordered ZnZrN₂ polymorph structures where $y = 1$ and $x = 0, 0.25, 0.50,$ and 0.75 . Details and structure matching are described in the SM [18].

To account for configurational degrees of freedom and associated entropic contributions to free energy, the “polymorph sampler” statistical approach of Stevanović *et al.* [2,23,24] was modified to include cation lattice disorder in the ZnZrN₂ system. The modification pertains mainly to structure classification and the statistical treatment; see Supplemental Material (SM) [18]. Using random structure sampling, we generated a set of 5000 random superlattice (RSL) ZnZrN₂ structures with 24-atom cells.

ZnZrN₂ structures approximating random disorder were simulated using the special quasirandom structure (SQS) method, which models random atomic decorations on a lattice in unit cells larger than most ordered structures but small enough to converge reliably with DFT [25]. This is achieved by searching for unit cells that reproduce or approximate pair (or higher-order) correlation functions by minimizing an objective function (see SM [18]). We calculated a set of SQS structures with 64 atoms for each ZnZrN₂ structure class using the ATAT package [26–28], selecting only structures with the lowest objective functions. Each SQS structure was assigned to its closest structure prototype class via a structure-matching algorithm to account for any SQS structures that may have relaxed to a different geometry.

D. First-principles calculations

Density functional theory (DFT) calculations were performed using the projector augmented wave (PAW) method [29,30] as implemented in the Vienna *ab initio* simulation package (VASP) [31,32], first within the Perdew-Burke-Enzerhof (PBE) generalized gradient approximation (GGA) formulation of the exchange-correlation functional [33]. Cutoff, convergence, and correction criteria are described elsewhere [34,35]. To estimate energetic contributions from vibrational degrees of freedom for structures of interest, density functional perturbation theory (DFPT) calculations for gamma (Γ) point phonons ($q = 0$) are run on representative polymorphs (see SM [18] for details).

The ordered ZnZrN₂ polymorph structures, 64-atom SQS structures, and alloy calculations ($x = 0, 0.25, 0.5, 0.75$), were relaxed first with a PBE functional, then with PBE using a Hubbard U correction (“PBE+ U ”) of 3 eV/atom for Zr as benchmarked by Stevanović and coworkers [36], and also with the SCAN meta-GGA functional, which has been demonstrated to more accurately predict polymorph orderings with the tradeoff of a higher computational cost [14,37,38]. The SCAN results are reported for all calculations herein, except for DFPT which uses PBE+ U and the polymorph sampler structures which were relaxed using PBE+ U since SCAN is too computationally expensive for 5000 structures. Additional calculation details are reported in the SM [18].

III. RESULTS

A. Identification of possible ZnZrN₂ polymorphs

Although only the WS phase is reported in the Materials Project database (ZrZnN₂, “mp-1014244”) [35,39], this unexplored Zn-Zr-N phase space could in principle host a variety of different structures. Many methods exist to determine possible polymorphs and predict synthesizable compounds [40],

ranging from simple ionic substitution [41] to kinetically limited minimization (KLM) [22], *ab initio* random structure searches (AIRSS) [42], or more expensive evolutionary and genetic algorithms [43]. Since no single method is fully representative of configurational space, we use the combined methods of KLM [22], random structure searching [2], and ionic substitution [14] to predict 28 unique possible ordered ZnZrN₂ polymorphs (three of which have been added to the NRELMatDB [36,44,45]). Most of these polymorphs have unit cells of 16 atoms or fewer and represent various orderings, and thus are referred to as “ordered” polymorphs herein.

The resulting 28 polymorphs are classified into six distinct structure prototype classes, with representative crystals for each of these structure prototypes depicted in Fig. 1(a), and adopt a naming convention from binary analogs as follows: rocksalt-derived (“RS”) is an fcc anion sublattice with cations in O_h-coordinated voids, wurtzite-derived (“WZ”) exhibits a structurally face-centered tetragonal anion lattice with tetrahedral coordinated cations, zinc-blende-derived (“ZB”, i.e., chalcopyrite) is an fcc anion sublattice with cations in every other tetrahedral void, wurtsalt (“WS”) presents alternating layers of octahedrally coordinated Zr and tetrahedrally coordinated Zn (as discussed previously), and boron-nitride-derived (“BN”) exhibits hexagonal sheets of various stackings (similar to graphite, but a 3D structure with *M*-N bonds between *c*-axis layers and the key distinction that the *c*-axis bond lengths are nearly equal to the in-plane bond lengths [46]). An additional compound, with alternating 2D layers corresponding to layers of the mineral litharge (PbO, with a space group *P4/nmm*) and the mineral massicot (PbO, with a space group *P2₁ca*), respectively, we name with the amalgam “lithicot” (“LC”; we were also unable to locate an existing mineral name). The heavily distorted versions of three of these prototypes are categorized separately, with the prefix “d,” using a tolerance developed from a structure matching algorithm; see SM [18] for classification scheme details. The structure class “d-HX” (HX = hexagonal) represents structures that are distortions between BN and WZ, which are related to one another through a displacive transformation. Zn₃N₂ crystallizes in an antibixbyite-derived phase (“BX”), which is observed experimentally, but this structure is not included in our set of prototypes since deriving an analogous topotactic ZnZrN₂ BX structure requires removing atoms and is not trivial.

The resulting 0-K formation energy of a given ordered polymorph in structure class *k* is referred to as ΔH_k^{ord} (e.g., $\Delta H_{\text{WS}}^{\text{ord}}$, $\Delta H_{\text{RS}}^{\text{ord}}$, etc.). Figure 1(b) plots the resulting energy ordering of the 28 ordered structures, with polymorphs grouped by structure type and “ E_{hull} ” indicating the energy above the convex hull, i.e., the difference between the computed ΔH_k^{ord} and the ground-state hull. The SCAN functional confirms a predicted ground-state WS (*P3m1*) that lies on the convex hull, corroborating the literature [3,9]. Other WS polymorphs (*P6₃mc*, *P3m1*) are low in energy, ranging from 0 to 0.025 eV/atom, and the LC structures (*Pca2₁*, *Iba2*) are the next lowest in energy. RS polymorphs are the highest in energy, with E_{hull} values ranging from 0.080 to 0.156 eV/atom. PBE and PBE+*U* yield similar energy orderings (see SM [18]), although LC is the predicted ground state for PBE without a Hubbard *U* correction (see SM [18]).

TABLE I. Representative ordered polymorphs from each prototype class with the lowest E_{hull} (see SM [18] for full list of polymorphs and energies).

Prototype class <i>k</i>	Space group	No. of atoms ^a	E_{hull} (eV/atom)	E_G (eV)	E_G^d (eV)	m_e^*	m_h^*
WS	<i>P3m1</i>	4	0.0	2.47	3.10	7.30	1.69
LC	<i>Pca2₁</i>	16	0.0106	1.63	1.63	1.33	1.87
d-HX	<i>P2₁/c</i>	16	0.0294	2.62	2.71	3.88	2.16
d-WS	<i>Cm</i>	32	0.0312	2.18	2.18	1.56	1.25
BN	<i>Cm</i>	16	0.0327	2.01	2.01	1.36	1.49
d-RS	<i>Pc</i>	16	0.0373	2.22	2.47	3.41	2.17
WZ	<i>Pmc2₁</i>	8	0.0496	2.53	3.23	0.62	3.62
RS	<i>I4₁/amd</i>	16	0.0807	1.15	1.87	0.83	1.96
ZB	<i>P4m2</i>	4	0.0857	2.04	3.03	0.52	1.59

^aNumber of atoms in primitive unit cell.

The E_{hull} values of the lowest-energy ordered structure in each prototype class, as well as their calculated band gaps (E_G) and electron and hole effective masses (m_e^* and m_h^*) from SCAN, are reported in Table I, with the full list in the SM (note that reported E_G are Kohn-Sham gaps calculated with SCAN, which systematically underestimates the true band gap [47]). Optoelectronic properties vary significantly by structure. Most polymorphs have indirect gaps except for the LC structures, most of the BN, some distorted structures, and one RS. The WZ *Pna2₁* polymorph exhibits the largest band gap ($E_G \approx 2.99$ eV with SCAN; see SM [18]), followed by d-HX, WS, ZB, d-RS, and d-WS with $E_G > 2$ eV, while RS has among the lowest band gaps (~ 0 –1.67 eV, depending on cation ordering). Notably, the lowest-energy WS *P3m1* polymorph has an exceptionally low m_h^* (< 2) compared to m_e^* (< 7) while retaining a wide direct band gap $E_G^d > 3$ eV. This combination of electronic structure properties is unique among all the considered polymorphs, and is rare for other chemistries outside of the ZnZrN₂ material system.

B. Synthesis of metastable phases

Despite the existence of at least 19 predicted polymorphs with lower 0-K DFT formation energies, an RS phase with a high E_{hull} is experimentally synthesized at low deposition temperatures (T_{dep}) and ZnZrN₂ stoichiometry. Using combinatorial sputter synthesis [48], a set of approximately 400 samples in the Zn_{*x*}Zr_{1-*x*}N_{*y*} ternary alloy system is grown, with cation concentration ranging from $0 \leq x \leq 1$ and growth temperature T_{dep} ranging from ambient to 500 °C. Figure 2(a) depicts RBS anion-to-cation ratio— $y = \text{anion}/(\text{Zn} + \text{Zr})$ with anion = (O+N), N, or O—as a function of cation ratio, $x = \text{Zn}/(\text{Zn} + \text{Zr})$, for a set of representative samples grown at ambient temperature. RBS corroborates the cation concentration measured by XRF and indicates N-rich compositions in Zn-poor samples, N-poor compositions in Zn-rich samples, and approximately stoichiometric N at the ZnZrN₂ composition of interest. Additionally, a small but nonzero presence of O is detected, likely substituting for N and plausibly residing on the film surface (~ 0.3 at. % in Zn-poor samples, ~ 5 at. % in Zn-rich samples due to reaction of zinc nitride with ambient atmosphere; see SM [18]). An exponential fit suggests our samples have crystallized near the

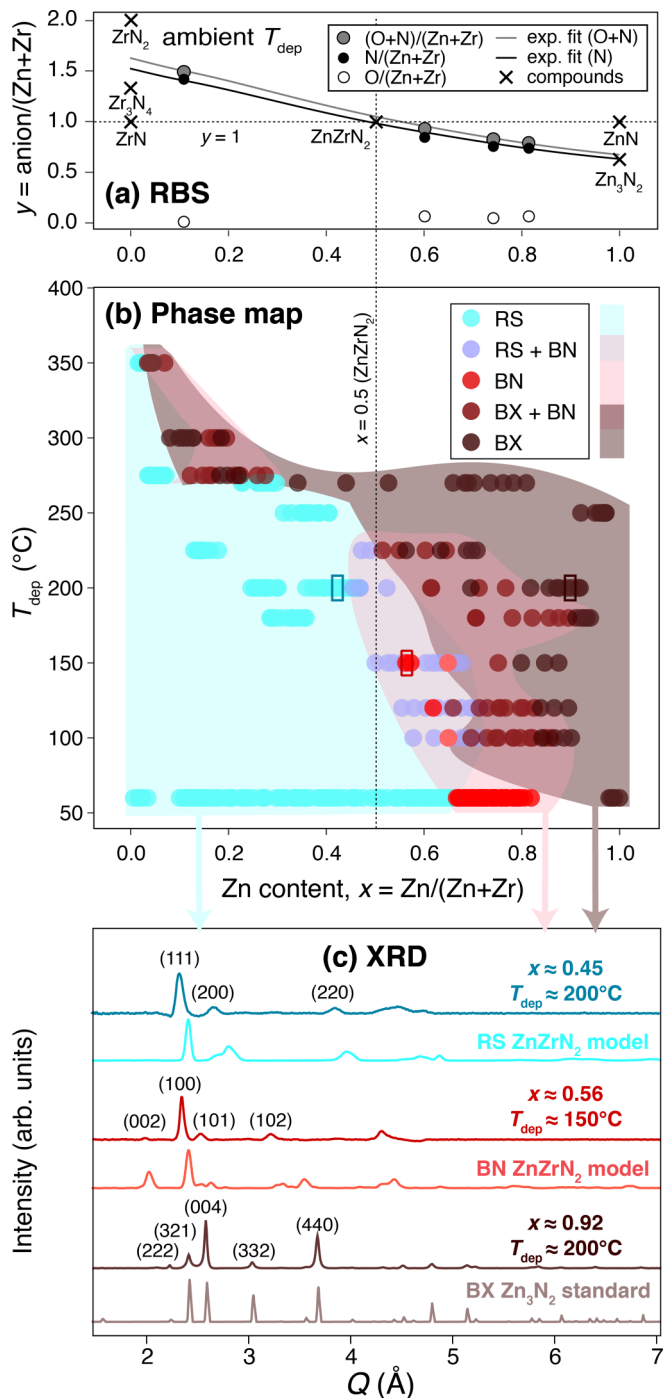


FIG. 2. (a) RBS measurements of anion composition as a function of cation composition, with exponential fits plotted. (b) Map of over 400 samples in Zn-Zr-N experimental phase space, with cation composition $x = \text{Zn}/(\text{Zn} + \text{Zr})$ on the x axis and calibrated deposition temperature T_{dep} on the y axis. (c) Representative XRD patterns for three samples marked with rectangles in (b), with “modeled” ZnZrN_2 RS and BN from ensemble averages of XRD patterns from the polymorph sampler method for ZnZrN_2 compositions, and “standard” Zn_3N_2 antixbybite (BX) from the Materials Project database plotted with a smearing bandwidth.

Zr_3N_4 – Zn_3N_2 tieline, as indicated by the exponential fit to RBS referenced to the crossed markers, with an approximate

stoichiometry of $\text{Zn}_x\text{Zr}_{1-x}\text{N}_y$, where $y \approx (4 - 2x)/3$. This system could alternately be expressed as “ $\text{Zn}_{1+x}\text{Zr}_{1-x}\text{N}_{2+y}$ ” to emphasize off stoichiometry from ZnZrN_2 (see SM [18]). For simplicity and generality we will refer to experimental alloys as “ $\text{Zn}_x\text{Zr}_{1-x}\text{N}_y$ ” herein since multiple experimental phases are observed, and focus on varying x since the anion composition y is not intentionally tuned.

Using high-throughput synchrotron XRD, and referencing the XRD patterns from the set of predicted polymorphs, the structural phase space is mapped in Fig. 2(b) by linking the structure of each of the ~ 400 samples to its corresponding ternary composition and calibrated deposition temperature T_{dep} . Rather than crystallizing in its predicted ground-state WS structure at and around the ZnZrN_2 ($x = 0.5$) composition, synchrotron XRD demonstrates predominantly an RS crystal structure, corresponding to an E_{hull} of at least 0.08 eV/atom according to Fig. 1. The transformation to a second phase is observed at higher x compositions, a hexagonal structure corresponding to BN (or possibly d-HX), and a third antixbybite-derived phase (BX) is observed at the highest x concentrations near Zn_3N_2 (simulating BX ZnZrN_2 is non-trivial and is not performed here). At higher T_{dep} , there are regions of mixed phases of these three polymorphs, perhaps due to miscibility or Zn volatility. We attempted to synthesize Zn-rich samples at $T_{\text{dep}} > 250^\circ\text{C}$, but no such samples were realized due to the high vapor pressure of Zn under our growth conditions (see SM [18]).

Figures 2(b) and 2(c) represent the key structural observations in $\text{Zn}_x\text{Zr}_{1-x}\text{N}_y$. First, an RS-derived phase dominates from $x = 0$ up to a threshold x value, which is approximately $x \approx 0.66$ at ambient temperature growth conditions ($T_{\text{dep}} \approx 65^\circ\text{C}$, bottom of figure) and which drops as T_{dep} increases. An XRD pattern for a representative RS sample of $x \approx 0.45$ is depicted in Fig. 2(c) in dark teal, compared to a modeled RS XRD pattern in light teal, simulated as ensemble averages from the polymorph sampler. The RS-derived phase at $x = 0$ is more N rich than RS ZrN , so we refer to it as ZrN_y ($y > 1$). This could in principle be a single or mixed phase of RS ZrN_y ($y > 1$), Zr_3N_4 [49,50], ZrN_2 , Zr_3N_2 [1,51], or $\text{Zr}_2\text{N}_{3-y}$ ($y = 0.34$) [52], with possible defect-mediated or oxygen-induced stabilization; in-depth investigation of this phase is beyond our scope. As the Zn content increases, the XRD peaks around $Q = 2.3$ and 2.65 \AA , which correspond to RS (111) and (200), respectively (indices from the ZrN RS structure; see SM [18]), shift to higher- Q values, with the former strengthening and the latter weakening. This tradeoff is likely due to shifts in texturing, as also commonly observed in other ternary nitrides [53].

At a threshold composition ($x \approx 0.66$ at ambient temperature), there is a phase transformation to a hexagonal BN-derived structure. Figure 2(c) depicts a representative BN diffraction pattern for a sample with $x \approx 0.56$ in dark red, with diffraction peaks at Q values of ~ 2.10 , 2.45 , and 2.55 \AA corresponding to BN (002), (100), and (101) reflections, respectively. This transformation occurs at lower x values for samples grown in the approximate range $100^\circ\text{C} \lesssim T_{\text{dep}} \lesssim 225^\circ\text{C}$, with a large region of mixed phase RS and BN (“RS + BN”).

At a second threshold composition ($x \gtrsim 0.8$ at ambient temperature, and lower x for high T_{dep}), a second phase

transition occurs to the BX phase which holds until $x = 1$ with a stoichiometry of approximately Zn_3N_2 . The presence of BX Zn_3N_2 corroborates literature reports [54] and may be enabled by Zr_{Zn} antisite stabilization across phase space. There are several regions of phase-segregated BX as well, in particular at $T_{\text{dep}} > 250^\circ\text{C}$. Here, films are likely completely phase separating into binaries of RS ZrN_y and BX Zn_3N_2 , though it is also plausible that a BX-derived phase of ZrN_y or Zr-rich Zn-Zr-N has formed and is responsible for the BX reflections.

In summary, RS and BN are synthesized near the ZnZrN_2 composition ($x = 0.5$) and BX at high x , but no WS phase is observed. The measured and simulated XRD patterns correspond very well, except for offsets in Q that are a consequence of errors in DFT lattice constants or experimental artifacts (e.g., off stoichiometry, possible residual strain, sample misalignment). It is notable that in this alloy system $\text{Zn}_x\text{Zr}_{1-x}\text{N}_y$, the presence of a lower-density hexagonal phase (BN, here) located between two higher-density cubic phases (RS and BX, here) is indicative of a phenomenon in heterovalent heterostructural alloys called “negative pressure” polymorphs [55,56], and this space warrants further exploration.

C. Statistical sampling of thermodynamically accessible polymorphs

The synthesis of metastable polymorphs (RS and BN) rather than the predicted ground state (WS) is not particularly surprising; DFT is a 0-K, thermodynamic equilibrium modeling approach of bulk systems while sputtering is a high effective-temperature, nonequilibrium synthesis approach of thin films, and so the two methods are not necessarily compatible. Despite these incompatibilities, DFT often *does* correctly predict sputtered crystal structures, for example, in other ternary nitrides [10] or in numerous oxide compounds, and thus is commonly used for simulating such materials. However, there are also other cases in the literature where the predicted DFT ground state is not synthesizable via sputtering or where sputtering can access metastable states. For example, ternary nitride ZnMoN_2 is predicted in a layered structure but synthesized in a WZ structure [57], Mg_2NbN_3 is predicted in a layered structure but synthesized in a RS structure [12], and Zn_2SbN_3 and Mg_2SbN_3 are metastable with respect to decomposition into N_2 yet both can be made by sputtering [58,59].

It is still not understood, for a given system, whether the DFT ground state will ultimately be synthesizable as a sputtered thin film or whether a higher-energy polymorph will crystallize instead, and in each case why or why not. Modeling sputtering from first principles is computationally difficult (e.g., time-dependent or Monte Carlo simulations), and is further complicated since sputtered films tend to decompose before equilibrium is reached. The computational analysis herein seeks to contextualize our experimental findings by assessing whether metastable states could be accessible experimentally using nonequilibrium synthesis techniques such as sputtering. These computational methods and the following discussion are *not* aimed to show that WS cannot be synthesized (it may very well be possible to synthesize WS under different conditions) but rather, we provide a rationale

for why metastable phases have been stabilized under these experimental conditions.

It has previously been shown that treating a spectrum of structures generated by random structure sampling [42] as a proper statistical ensemble can determine the experimental realizability of metastable crystalline polymorph phases (e.g., MgO, ZnO, SnO_2 , and Si) [2,23] as well as the structural features of glasses [24]. Here, 5000 ZnZrN_2 RSL structures are generated with random structure sampling, and the resulting spectrum of polymorph structures is split into prototype classes with the same underlying space group (see SM [18]). Next, the ensemble probability P_k of every individual class is evaluated as

$$P_k \approx \frac{\sum_{n=m}^{m+n_k} \omega_n e^{-\frac{E_{\text{hull},n}}{k_B T_{\text{eff}}}}}{\Xi} = \frac{\Xi_k}{\Xi}, \quad (1)$$

where k represents different prototype classes, n counts polymorph structures within a given class, ω_n is the frequency of occurrence of a structure n belonging to class k , $E_{\text{hull},n}$ is the formation energy per atom relative to the ground state, and T_{eff} is the effective temperature as described in Eq. (2) subsequently. Ξ_k and Ξ are the partial and the full partition functions, respectively. The former pertains only to the k class of structures, while the latter is evaluated for all RSL structures. We use the “ \approx ” symbol to emphasize that the ensemble probabilities from Eq. (1) are the approximate versions of the true ensemble probabilities (only configurational degrees of freedom are sampled). All of the approximations adopted in the polymorph sampler approach are discussed and analyzed at length by Jones and Stevanović [24].

The thermodynamic density of states (TDOS; i.e., number of structures per energy unit) resulting from the random structure sampling, normalized and resolved by structure class, is shown in Fig. 3(a). Two features become immediately apparent. First, consistent with Fig. 1(b) and literature reports, the ground-state WS structure is correctly identified (dark gray), but its corresponding frequency of occurrence and associated TDOS are very small. Second, RS structures have the largest TDOS peak (cyan), concentrated in the narrow window of 0.08–0.12 eV/atom. This suggests the flexibility of RS to accommodate cation disorder in a relatively narrow energy interval. Additional classes of disordered structures with more significant occurrence are the BN (red) and the two highly distorted d-RS and d-WS classes (striped), with the latter also including structures with more than one tetrahedral layer sandwiched between the octahedrally coordinated layers of the WS structures. It is also important to note that none of the other previously discussed structure classes appear in the RSL structures, including the LC and WZ classes with DFT formation energies lower than that of RS. This indicates that all possible structures in these absent classes exhibit very “narrow” local minima in configurational energy space, leading to a very low probability of occurrence. The same is true for a relatively large number of very low-symmetry structures (space groups $P1$ and $P\bar{1}$) typically obtained in random structure sampling, but since none of these structures occur in large numbers they become statistically insignificant compared to those depicted in Fig. 3.

The TDOS from Fig. 3(a) allows evaluating ensemble probabilities per Eq. (1) and associated partial partition

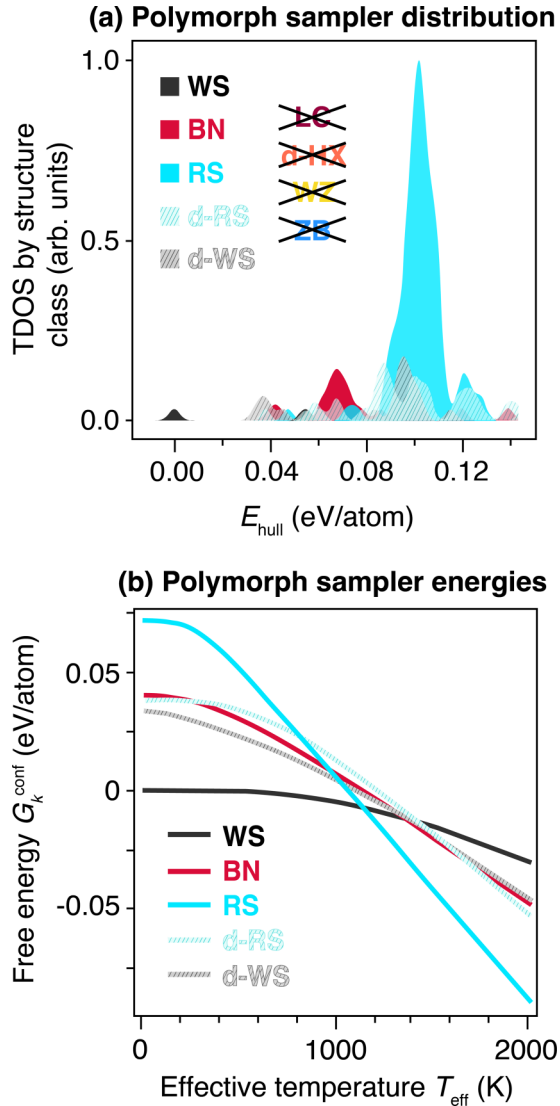


FIG. 3. (a) Thermodynamic density of states (TDOS) distribution of sampled ZnZrN_2 polymorphs from random structure searching, demonstrating a dominant RS peak, as calculated from Eq. (1). Crossed-out classes depicting the absence of several predicted polymorph phases. (b) Free energy G_k^{conf} as a function of effective temperature T_{eff} , shifted such that the ground state at $T_{\text{eff}} = 0$ K is at the origin, calculated from the TDOS using Eq. (2).

functions Ξ_k . These are used to evaluate the configurational free energies G_k^{conf} of the corresponding structure types using the standard statistical mechanics equation

$$G_k^{\text{conf}}(T_{\text{eff}}) = -k_B T_{\text{eff}} \ln \Xi_k, \quad (2)$$

where k_B is the Boltzmann constant.

T_{eff} is the “effective temperature,” defined in the literature as the thermodynamic temperature where a material grown *in* equilibrium would have the same degree of disorder as the same material grown *out* of equilibrium (e.g., by sputtering) [60,61]. Effective temperature T_{eff} can be thought of as a proxy for disorder, such that higher T_{eff} represents higher disorder in a given material. The T_{eff} models configurational disorder as typically seen in nonequilibrium synthesis. T_{eff} and T_{dep} are not directly comparable; rather,

low-deposition temperatures generally correspond to high T_{eff} because kinetic limitations inhibit enthalpy-driven ordering (see Sec. IV b). Accordingly, the corresponding free energy G_k^{conf} excludes nonconfigurational free-energy contributions such as vibrational contribution (see Sec. III d) [61]. Also, the ideal gas free energy of N_2 , which is otherwise by far the largest finite-temperature free-energy contribution under thermodynamic equilibrium conditions (up to several eV, depending on temperature and partial pressure), does not apply in sputtering synthesis, where high nonequilibrium nitrogen chemical potentials up to $\Delta\mu_{\text{N}} = +1.0$ eV can be achieved [62].

The resulting T_{eff} dependence of the free energy G_k^{conf} , displayed in Fig. 3(b), clearly shows that at low T_{eff} the lowest free-energy structure is the ground-state WS structure, consistent with Fig. 1. However, at $T_{\text{eff}} \gtrsim 1150$ K, the disordered RS becomes the most favorable structure due to the large gain in configurational entropy [63]. In the temperature range 1300–1600 K, the WS structure gives way to disordered BN as the second most favorable structure, while at still higher temperatures the d-RS becomes the most favorable. This structure, if mixed with RS, would be experimentally difficult to distinguish from RS using XRD because of their very similar diffraction patterns.

In summary, at higher effective temperatures the polymorph sampler ensemble treatment suggests the following ordering of structures according to G_k^{conf} , from lowest to highest: (1) RS, (2) distorted RS (d-RS), (3) BN, (4) distorted WS (d-WS), and (5) WS. This is consistent with our experimentally observed XRD patterns that are compared with the ensemble-averaged patterns in Fig. 2(c). We reiterate that T_{eff} is representative of *effective* temperature rather than T_{dep} , the substrate temperature during sputter synthesis. Previous studies have suggested that sputter deposition occurs at T_{eff} higher than 1150 K in ternary nitrides; in fact, T_{dep} has been shown to scale *inversely* with T_{eff} for sputtered films (where $T_{\text{dep}} \lesssim 600$ °C) since strong kinetic limitations at low T_{dep} induce a high degree of disorder (see SM [18]) [64,65]. Therefore, since computed phases at high T_{eff} correspond to phases grown at low T_{dep} in Fig. 2, these ensemble probabilities and free energies support the observed behavior in sputter-deposited samples: the RS phase is stabilized and the WS phase is destabilized.

D. Vibrational contributions are negligible

We have highlighted the role of configurational degrees of freedom in this system. However, it is also important to assess whether other energetic contributions, in particular vibrational contributions, significantly change energy ordering. Here, we use DFPT to estimate energetic contributions from vibrational degrees of freedom for the lowest-energy RS, BN, and WS phases of ZnZrN_2 , and report the resulting Gibbs free energy G_k^{vib} (details provided in the SM [18]). It is noted that the G_k^{vib} is a function of the actual synthesis temperature T (i.e., T_{dep} up to about ~ 630 K here), rather than the effective temperature T_{eff} discussed in the polymorph sampler approach [61,66]. These results show that RS is somewhat destabilized with respect to BN at very high temperatures ($T \approx 1800$ K), but across all assessed temperatures WS is still the lowest-energy

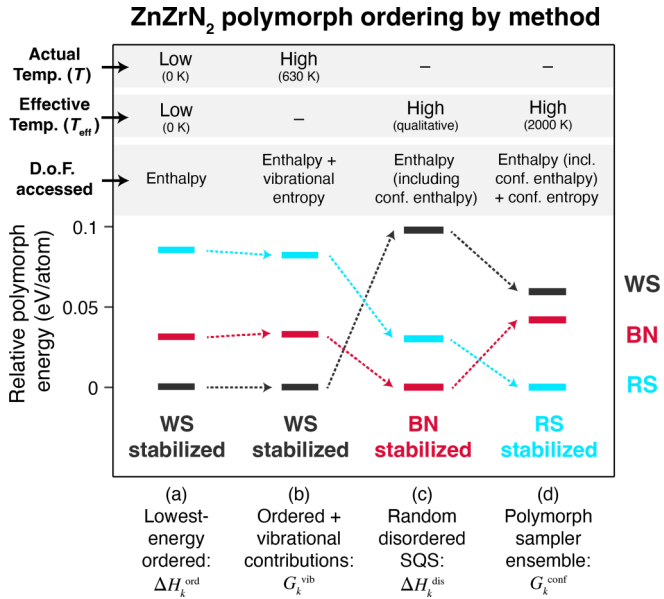


FIG. 4. Comparison of relative polymorph energy orderings by calculation method for WS, BN, and RS structure classes, from left to right: (a) enthalpies of lowest-energy ordered structures ΔH_k^{ord} (i.e., E_{hull} in Fig. 1), (b) free energies including vibrational contributions of ordered structures G_k^{vib} at $T = 630$ K, (c) enthalpies of disordered SQS structures ΔH_k^{dis} (from Fig. 5), and (d) the polymorph sampler free energies G_k^{conf} at $T_{\text{eff}} = 2000$ K (from Fig. 3). A qualitative metric (“low” or “high”) is reported for actual temperature T and effective temperature T_{eff} (a proxy for cation disorder, as explained in the text), and accessed degrees of freedom (DoF) are labeled (“conf” corresponds to configurational DoF). $T = 630$ K is selected for G_k^{vib} to represent the highest deposition temperature (T_{dep}) probed experimentally in this paper, rounded up to the nearest 10 K. Energy is referenced on the y axis with respect to the lowest formation energy for a given method, and arrows are a guide to the eye.

structure compared to RS or BN. At the highest experimentally probed temperature ($T_{\text{dep}} = 350^\circ\text{C}$, i.e., ~ 630 K), the relative change in the RS and BN polymorph energy due to vibrational effects is approximately 3–4 meV/atom, which is much smaller than the polymorph sampler energy differences observed at high T_{eff} in Fig. 3(b). These energy differences are depicted in Fig. 4 by comparing the relative energy ordering between (a) ΔH_k^{ord} , (b) G_k^{vib} , and (d) G_k^{conf} , and are elaborated upon in the discussion section. Therefore, vibrational effects do not explain the stabilization of BN and RS over the WS phase observed in our experiments. Rather, by comparing to the configurational contributions to free energy, we show RS and BN are stabilized and WS is destabilized at high temperature by *configurational* degrees of freedom rather than vibrational degrees of freedom.

IV. DISCUSSION AND IMPLICATIONS

We have synthesized the RS-derived and BN-derived ZnZrN_2 structures rather than WS, which is the DFT-predicted ground state at 0 K, and have used a statistical polymorph sampler to explain these results by demonstrating that RS becomes the lowest-energy polymorph at high effective temperatures. However, this does not explain the physical

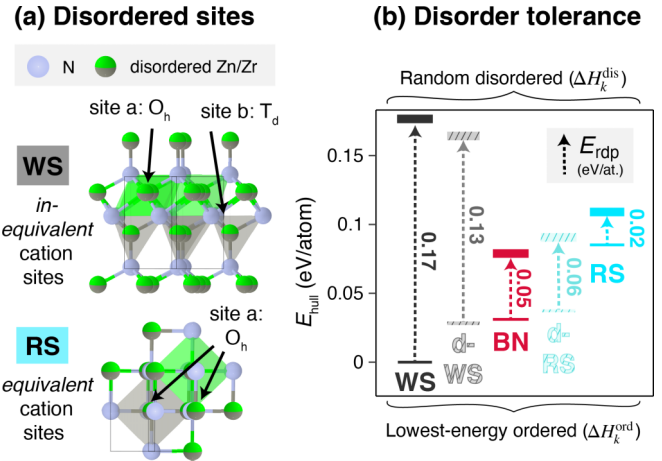


FIG. 5. (a) Schematic of the WS- and RS-derived structures with cation site disorder as an example of structures with inequivalent and equivalent cation sites, respectively. (b) Comparison of formation energies of the lowest-energy ordered polymorph structure (ΔH_k^{ord}) and of the random disordered structure (ΔH_k^{dis}) for each prototype class plotted in Fig. 3. The E_{rdp} descriptor is shown, with a lower E_{rdp} correlating to the higher-disorder tolerances in the BN and RS structures that are observed experimentally (see SM [18]).

principle behind why certain structures are stabilized or destabilized upon disorder, nor why BN is synthesized at Zn-rich compositions. Inspection of structures in Fig. 1(a) indicates that the ordered polymorph structures with lowest ΔH_k^{ord} exhibit unique, inequivalent cation coordination environments for Zr and Zn (WS, LC), while higher formation energy structures have similar, equivalent coordination environments for all cation sites (RS, BN, WZ, ZB). This is demonstrated in Fig. 5(a) with partially occupied WS and RS structures.

Our hypothesis is that cation disordering during synthesis, enabled by rapid condensation from the vapor state to the solid state in physical vapor deposition (PVD) techniques such as sputtering, favors structures with similar cation coordination environments, thus lowering the probability of the formation of WS. To examine this hypothesis and explore how the polymorph sampler results pertain to other systems, we pursue two high-throughput computational approaches. First, we develop a descriptor to interpret the results of the polymorph sampler within the framework of random cation disorder and, second, we estimate formation energies of ordered $\text{Zn}_x\text{Zr}_{1-x}\text{N}_y$ with varied cation ratios x to assess the effects of off stoichiometry in relation to experimental phase space.

A. Tolerance to disorder influences synthesizability at high effective temperatures

In practice, cation disorder is ubiquitous in ternary nitrides [65,67,68], especially in materials synthesized at high effective temperatures (as present in sputtering). Thus, modeling small, cation-ordered unit cells as in Fig. 1 may not adequately capture energetic information in these systems. Here, the energetic effects of random cation disorder in ZnZrN_2 polymorph structures are explicitly considered by generating random disordered structures in each structure class using the SQS method, as described previously. For each

structure class k , these resulting formation energies all are within ~ 0.010 eV/atom of one another; these energies are then ensemble averaged to best represent the formation energy of a randomly disordered phase, referred to as ΔH_k^{dis} .

Figure 5(b) compares ΔH_k^{dis} to the ΔH_k^{ord} of the lowest-energy ordered structures for the five structure classes that emerge from the polymorph sampler (see SM [18] for others), referenced to $\Delta H_{\text{WS}}^{\text{ord}}$ and reported as E_{hull} . The random disordered WS and d-WS structures have high formation energies, with $\Delta H_{\text{WS}}^{\text{dis}}$ over 0.17 eV/atom. In contrast, $\Delta H_{\text{RS}}^{\text{dis}}$ is lowest of all disordered structures. Although RS does not have the lowest ΔH_k^{dis} , $\Delta H_{\text{RS}}^{\text{dis}}$ is very similar (within 0.025 eV/atom) to $\Delta H_{\text{RS}}^{\text{ord}}$, and thus has a lower energetic penalty to disorder. To assess this “disorder tolerance” for a given structure class k , we introduce a descriptor, the “random disordered polymorph energy” E_{rdp} :

$$E_{\text{rdp}}(k) = \Delta H_k^{\text{dis}} - \Delta H_k^{\text{ord}}. \quad (3)$$

RS and BN, the structures that have been experimentally synthesized, have the lowest E_{rdp} values. Physically, since the 0-K DFT formation energy is an approximation of formation *enthalpy*, the E_{rdp} represents the *additional enthalpy* that is introduced for each structure as a result of cation disorder. This is the change in enthalpy as a result of geometric distortions and high-energy bonds induced by disorder, rather than entropic effects. Thus, we have shown that in the ZnZrN_2 polymorph structures with inequivalent cation sites (WS, LC), cation disordering significantly increases enthalpy, whereas in the ZnZrN_2 structures with equivalent cation sites (RS, BN) cation disordering only negligibly increases enthalpy.

Four computational methods and resulting sets of energies have been considered so far: DFT to compute formation energies of ordered structures in Fig. 1(b) (ΔH_k^{ord}), DFPT to estimate vibrational contributions in the SM [18] (G_k^{vib}), SQS to estimate random disordered structures in Fig. 5(b) (ΔH_k^{dis}), and the polymorph sampler ensemble to model configurational degrees of freedom in Fig. 3(b) (G_k^{conf}). Since an SQS structure approximates configurational disorder, it is also representative of a disordered structure that might be observed at high T_{eff} . Thus, the ΔH_k^{dis} represent similar disordered structures as the G_k^{conf} at sufficiently high T_{eff} (e.g., at $T_{\text{eff}} = 2000$ K, chosen as a representative high T_{eff} as depicted in Fig. 3), with the former accessing enthalpy and the latter accessing enthalpy and entropy. Figure 4 shows that the relative polymorph ordering changes across the four methods: WS is lowest in ΔH_k^{ord} and G_k^{vib} (at “high” temperatures of $T = 630$ K), disordered BN is lowest in ΔH_k^{dis} , and RS is lowest in G_k^{conf} (at “high” effective temperatures of $T_{\text{eff}} = 2000$ K).

Since G_k^{conf} includes both enthalpic *and* entropic degrees of freedom, and ΔH_k^{dis} includes only enthalpic degrees of freedom, comparison of Figs. 4(c) and 4(d) suggests that at high disorder the RS phase is *entropically stabilized* compared to BN. Meanwhile, at high disorder the WS phase is *enthalpically destabilized* compared to the RS and BN phases. We reiterate that vibrational effects as shown in Fig. 4(b) do not induce significant energetic reordering. Distorted structures (d-RS and d-BN) are excluded from Fig. 4 for clarity, though none of them are the lowest-energy structure in any of these calculations. We acknowledge that the SQS disordered

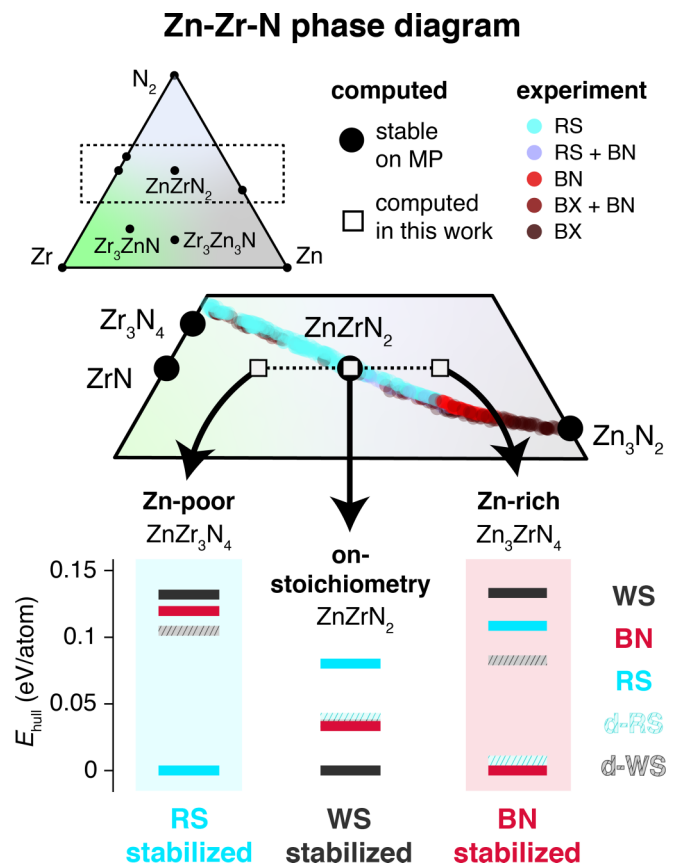


FIG. 6. Ternary phase diagram of Zn-Zr-N and a closeup of the $\text{Zn}_x\text{Zr}_{1-x}\text{N}$ region, with computed compounds from the Materials Project designated. Colored circles depict the approximate composition and associated phases of experimental data from this work (see Fig. 2). Computed compositions from this study are represented with unfilled squares in the phase diagram, and for each composition the lowest formation energy structure for a given class is plotted with colored bars.

structures that determine ΔH_k^{dis} are estimates (for example, a cluster expansion could be fit to rigorously account for short-range order and obtain a more accurate estimate), but ultimately these estimates support the hypothesis that disorder tolerance stabilizes the RS and BN phases over other considered polymorphs at high effective temperatures. Additionally, we have distinguished which stabilization effects are due to changes in enthalpy and which are due to changes in configurational entropy.

B. Tolerance to off stoichiometry informs phase transitions

It has been suggested why RS and BN are stabilized with sputtering, but it is not yet understood why RS is synthesized at Zr-rich compositions and BN at Zn-rich compositions. Another plausible explanation for the absence of WS ZnZrN_2 is that it is a “line compound,” a phenomenon observed in other ternary nitride systems such as $\text{ZnSnN}_2:\text{ZnO}$ [69]. A line compound is stable only in a very narrow region of configurational space such that it may be missed using combinatorial growth.

Figure 6 plots ternary Zn-Zr-N phase space, which constitutes configurational space in this system, and shows

approximately where experimental samples lie with respect to computed phases. To explore this hypothesis, we perform cation substitution in each of the ordered ZnZrN_2 polymorph structures from Fig. 1 to create a set of prototypes across the ZrN-ZnN tieline, i.e., $\text{Zn}_x\text{Zr}_{1-x}\text{N}_y$, where $y = 1$ and $x = 0.25, 0.50, 0.75$ ($x = 0$ in SM), and then relax the structures (note that these are small ordered unit cells, not SQS cells). This constitutes a very rough alloy approximation since sputtered films are N-rich for $x < 0.5$ and N-poor for $x > 0.5$; the experimental alloy is closer to the $\text{Zr}_3\text{N}_4\text{-Zn}_3\text{N}_2$ tieline, but this heterovalent alloy is far trickier to model due to defect compensation and is not performed here.

Relative polymorph stability for relevant structure classes with $E_{\text{hull}} < 0.15$ eV/atom is depicted for ZnZr_3N_4 , ZnZrN_2 , and Zn_3ZrN_4 in Fig. 6 (see SM [18] for hull stability plots and all classes). WS is highly destabilized in Zn-poor and Zn-rich cases, suggestive of a line compound. RS is the lowest-energy polymorph for a wide window of Zn-poor compositions and BN is the lowest-energy polymorph in Zn-rich compositions (see SM [18]). Since the LC, ZB, and WZ phases do not emerge in the polymorph sampler and given that WS is highly metastable at high T_{eff} (see Fig. 3), at high T_{eff} we would expect a phase change from RS to BN somewhere within approximately $0.45 < x < 0.55$ (see SM [18]), which corroborates experimental findings. These calculations use the nominal valence of the cations, namely, Zn^{2+} and Zr^{4+} ; we do not perform defect calculations nor vary cation oxidation states. Rigorous examination of alloy phase space would require an in-depth calculation of a temperature-dependent phase diagram, which is beyond our scope. However, this simple approximation is sufficient to explain our experimental observation of a phase change from RS to BN as x increases in $\text{Zn}_x\text{Zr}_{1-x}\text{N}_y$ at high T_{eff} . This is supported by the previous discussion on disorder tolerance: in order to achieve off stoichiometry, cations have to be placed on energetically unfavorable sites.

C. Implications for materials discovery

Although neglected in this analysis, dynamic, kinetic, and additional entropic effects may play a role in this ternary phase space. Electronic contributions to entropy have shown to be negligible in solid alloys [70]. As has been demonstrated in other II-IV-N₂ systems, spurious oxygen incorporation from the growth chamber can influence phase stability and result in impurity phases [14], though our $\text{O}/(\text{Zn}+\text{Zr})$ values below 1% from Fig. 2(a) suggest that a phase-segregated oxide is not observed here. Additionally, the elemental Zr used in our sputter target contains ~ 10 at. % Hf, which could influence relative phase stability. Finally, surface morphology, templating during growth, and kinetic effects could be assisting in restricting the formation of WS, and in enabling the preferential formation of RS and BN. Even though these films are grown on amorphous fused silica, we also acknowledge the possibility of preferential nucleation. These factors are all important to take into account in materials discovery studies.

There are many new predicted ternary nitrides and pnictides to explore beyond ZnZrN_2 [10]. However, an understanding of which polymorphs are actually synthesizable remains elusive. An assessment of the role of cation disorder

tolerance in emerging ternary pnictide systems is presented in Fig. 7, with the set of II-IV-V₂ pnictide semiconductors considered in Fig. 7(a) where II = (Ba, Mg, Ca, Be, Sr, Zn, Cd), IV = (Si, Ge, Sn, Pb, Ti, Zr, Hf), and V = (N, P, As). Theoretically, this set includes 147 unique compositions; as shown in Fig. 7(b), to date only 31 of these compositions have been confirmed experimentally and only 43 other predicted compositions are in the Materials Project (MP) database, leaving 73 II-IV-V₂ compositions not yet on the database at this time. Within the set of predicted but not-yet-synthesized compounds (yellow), Fig. 7(c) shows that at least two systems other than ZnZrN_2 have computed ground states where cations occupy symmetrically inequivalent lattice sites: SrGeN_2 (*Pbca*) and ZnHfN_2 (*P3m1*). This is also feasible for the 73 ternary pnictide compositions still missing from the MP database, leading to the experimental realizability of new metastable compounds with promising properties to be explored.

V. CONCLUSION

In summary, we have grown the first $\text{Zn}_x\text{Zr}_{1-x}\text{N}_y$ samples (a set of approximately 400 thin films) using combinatorial sputter synthesis, demonstrating the crystallization of metastable rocksalt-derived (RS) and boron-nitride-derived (BN) phases with cation-disordered structures, rather than the predicted cation-ordered “wurtsalt” (WS) ground-state phase. These findings have been explained using first-principles computational methods. By statistically sampling configurational degrees of freedom of polymorphs generated by random structure sampling, we demonstrate energetic destabilization of the predicted DFT WS ground state at high temperatures and stabilization of RS and BN phases that support our experimental results. It is shown that this stabilization can be attributed to the increased disorder tolerance in the RS and BN phases due to only minor gains in configurational enthalpy, suggesting that the RS phase is entropically stabilized to a higher degree than BN. Ordered alloy calculations of varying cation composition suggest that RS and BN have a higher tolerance to cation off stoichiometries compared to WS, predicting a phase transformation from RS to BN as x increases that corroborates our experimental findings. These results demonstrate the utility of sputtering in accessing high effective temperatures and synthesizing polymorphs predicted to be metastable within the DFT approximation at 0 K.

However, we acknowledge that growth methods and deposition conditions matter significantly in phase stabilization, and sputtering of thin films is just one synthesis approach. Although WS is energetically destabilized here by sputter synthesis, its realizability is not definitively ruled out. Future work on targeted synthesis of WS phases (e.g., low effective temperature, epitaxial, on-stoichiometry synthesis) is needed to assess whether WS is indeed synthesizable. If synthesizable, WS ZnZrN_2 holds promise as a piezoelectric material and for optoelectronic applications [15,71]. Furthermore, in-depth structural analysis and optoelectronic properties of the RS and BN polymorphs in this system remain to be investigated. Table I indicates promising properties for device applications such as contact materials, solar cell absorbers, photocatalysts, piezoelectric and

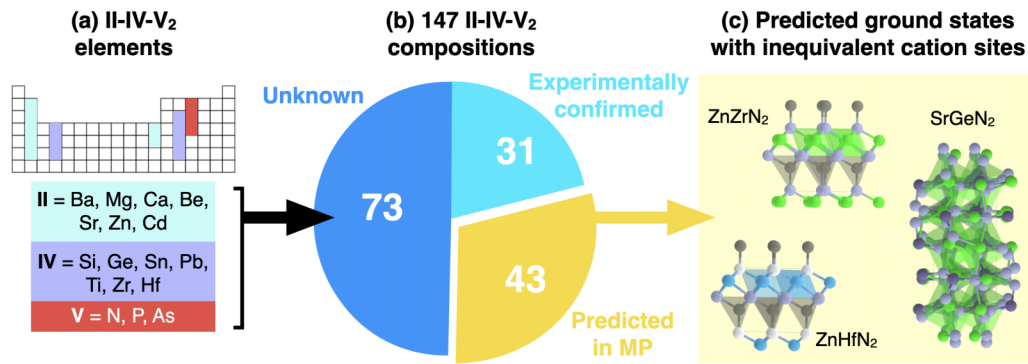


FIG. 7. Assessment of the role of cation disorder tolerance in emerging ternary pnictides. (a) Elements within the II-IV-V₂ composition space. (b) The distribution of composition spaces within the Materials Project (MP) database. (c) Three example systems from the “predicted in MP” category where cations occupy symmetrically inequivalent lattice sites.

ferroelectric materials [15,71]. In particular, the synthesized BN-derived polymorph has >2 eV band gap and low (<1.5) well-matched electron and hole effective masses, making it interesting for electronic devices that can operate at elevated temperatures. Additionally, this nonpolar BN polymorph is the transition state between two variants of the polar WZ structure, suggesting a pathway to tuning its predicted and measured ferroelectric response [72,73].

The results of this work suggest that other thermodynamically “metastable” materials according to 0-K DFT may be possible to synthesize. Presently, DFT is one of the most popular methods to generate high-throughput thermochemistry data with reasonable accuracy, despite the fact that zero-temperature formation energies provide only a rough estimate of actual material stability. In extended inorganic solids, a general rule of thumb is that entropy contributes on the order of ~ 0.05 – 0.1 eV/atom to the free energy. Accordingly, many high-throughput computational screening studies discard materials that have an E_{hull} above a cutoff of ~ 0.05 – 0.1 eV/atom. However, this study demonstrates synthesis of a RS polymorph phase with E_{hull} in the range of ~ 0.08 – 0.15 eV/atom using a common PVD technique, suggesting stabilization due to disorder tolerance. Since this phase would have been ruled out as not synthesizable by a typical high-throughput computational screening, it may be important to revisit what other metastable but synthesizable phases have been overlooked in such studies.

A contemporary challenge in materials science research is to bridge the gap between computationally predicted materials and experimental materials that can actually be grown in the laboratory with desired properties. The ZnZrN₂ results presented in this study are interesting beyond this specific material system because there may be many accessible energetic states that neither scientists nor nature have realized yet. In the Zn-Zr-N material system, it appears that tolerance to disorder and off stoichiometry contribute to the realization of high formation energy phases, and this study has introduced a descriptor (E_{rdp}) to assess disorder tolerance. However, in other material systems there may be different physical mechanisms enabling synthesis of metastable polymorphs. In general, the computational materials discovery community needs to continue to redefine the metrics by which phase stability and synthesizability are assessed in order to yield

experimentally realizable predictions that enable new functional materials.

All ordered crystal structures will be uploaded to the Materials Project database and available free of charge. Experimental data are available on the High Throughput Experimental Materials (HTEM) Database [76]. All data needed to evaluate the conclusions in the paper are present in the paper and/or the Supplemental Material [18].

ACKNOWLEDGMENTS

This work was authored in part at the National Renewable Energy Laboratory (NREL), operated by Alliance for Sustainable Energy, LLC, for the U.S. Department of Energy (DOE) under Contract No. DE-AC36-08GO28308. Funding was provided by the Office of Science (SC), Office of Basic Energy Sciences (BES), Materials Chemistry program, as a part of the Early Career Award “Kinetic Synthesis of Metastable Nitrides.” R.W.-R. acknowledges financial support from the U.C. Berkeley Chancellor’s Fellowship and the National Science Foundation (NSF) Graduate Research Fellowship under Grants No. DGE1106400 and No. DGE175814. V.S. acknowledges financial support from NSF Career Award No. DMR-1945010 for polymorph sampler ensemble calculations. S.L. acknowledges financial support from the U.S. DOE, SC, BES, as part of the Energy Frontier Research Center for Next Generation of Materials Design. Use of the Stanford Synchrotron Radiation Lightsource, SLAC National Accelerator Laboratory is supported by DOE’s SC, BES under Contract No. DE-AC02-76SF00515. The computational work in the Materials Project program (KC23MP) was supported by the U.S. DOE, SC, BES, Materials Sciences and Engineering Division under Contract No. DE-AC02-05-CH11231 (Materials Project program KC23MP). The authors thank Dr. S. Bauers, Dr. K. Talley, V. Jacobson, and R. Sherbondy for experimental assistance, Dr. S. Dwaraknath, Dr. E. Sivonxay, and M. McDermott for computational assistance, Dr. J. Perkins and Dr. A. Mehta with characterization assistance, and Dr. A. Tamboli and Dr. W. Sun for insightful discussions. This work used high-performance computing resources located at NREL and sponsored by the Office of Energy Efficiency and Renewable Energy. The views expressed in the article do

not necessarily represent the views of the DOE or the U.S. Government.

R.W.-R., A.Z., and K.A.P. conceptualized the work; R.W.-R., V.S., S.L., and K.N.H. were responsible for the methodology; R.W.-R., V.S., S.L., and M.K.H. conducted the computational investigation; R.W.-R., K.N.H., A.Z. con-

ducted the experimental investigation; R.W.-R. and V.S. were responsible for writing the original draft; R.W.-R., A.Z., S.L., M.K.H., and K.A.P. were responsible for reviewing and editing; R.W.-R., A.Z., V.S., and K.A.P. were responsible for funding acquisition; and A.Z., V.S., and K.A.P. were responsible for overall supervision.

- [1] W. Sun, A. Holder, B. Orvañanos, E. Arca, A. Zakutayev, S. Lany, and G. Ceder, *Chem. Mater.* **29**, 6936 (2017).
- [2] V. Stevanović, *Phys. Rev. Lett.* **116**, 075503 (2016).
- [3] W. Sun, S. T. Dacek, S. P. Ong, G. Hautier, A. Jain, W. D. Richards, A. C. Gamst, K. A. Persson, and G. Ceder, *Sci. Adv.* **2**, e1600225 (2016).
- [4] M. Aykol, S. S. Dwaraknath, W. Sun, and K. A. Persson, *Sci. Adv.* **4**, eaaq0148 (2018).
- [5] M. Aykol, V. I. Hegde, L. Hung, S. Suram, P. Herring, C. Wolverton, and J. S. Hummelshøj, *Nat. Commun.* **10**, 2018 (2019).
- [6] M. Horton, S. Dwaraknath, and K. A. Persson, *Nat. Comput. Sci.* **1**, 3 (2021).
- [7] P. Kroll, *J. Solid State Chem.* **176**, 530 (2003).
- [8] A. L. Greenaway, C. L. Melamed, M. B. Tellekamp, R. Woods-Robinson, E. S. Toberer, J. R. Neilson, and A. C. Tamboli, *Annu. Rev. Mater. Res.* **51**, 591 (2021).
- [9] Y. Hinuma, T. Hatakeyama, Y. Kumagai, L. A. Burton, H. Sato, Y. Muraba, S. Iimura, H. Hiramatsu, I. Tanaka, H. Hosono, and F. Oba, *Nat. Commun.* **7**, 11962 (2016).
- [10] W. Sun, C. J. Bartel, E. Arca, S. R. Bauers, B. Matthews, B. Orvañanos, B.-R. Chen, M. F. Toney, L. T. Schelhas, W. Tumas *et al.*, *Nat. Mater.* **18**, 732 (2019).
- [11] A. D. Martinez, A. N. Fioretti, E. S. Toberer, and A. C. Tamboli, *J. Mater. Chem. A* **5**, 11418 (2017).
- [12] S. R. Bauers, A. Holder, W. Sun, C. L. Melamed, R. Woods-Robinson, J. Mangum, J. Perkins, W. Tumas, B. Gorman, A. Tamboli *et al.*, *Proc. Natl. Acad. Sci. USA* **116**, 14829 (2019).
- [13] F. Kawamura, M. Imura, H. Murata, N. Yamada, and T. Taniguchi, *Eur. J. Inorg. Chem.* **2020**, 446 (2020).
- [14] A. L. Greenaway, A. L. Loutris, K. N. Heinselman, C. L. Melamed, R. R. Schnepf, M. B. Tellekamp, R. Woods-Robinson, R. Sherbondy, D. Bardgett, S. Bauers *et al.*, *J. Am. Chem. Soc.* **142**, 8421 (2020).
- [15] C. Tholander, C. Andersson, R. Armiento, F. Tasnadi, and B. Alling, *J. Appl. Phys.* **120**, 225102 (2016).
- [16] J. P. Dismukes, R. T. Smith, and J. G. White, *J. Phys. Chem. Solids* **32**, 913 (1971).
- [17] D. O. Scanlon and G. W. Watson, *Appl. Phys. Lett.* **97**, 131904 (2010).
- [18] See Supplemental Material at <http://link.aps.org/supplemental/10.1103/PhysRevMaterials.6.043804> for details about synthesis, characterization, polymorph, and DFT formation energy ordering, and computational methods [2,19,20,23,24,35,66,74,75].
- [19] A. Subramanian, J. D. Perkins, R. P. O'Hayre, S. Lany, V. Stevanovic, D. S. Ginley, and A. Zakutayev, *APL Mater.* **2**, 022105 (2014).
- [20] A. N. Fioretti, A. Zakutayev, H. Moutinho, C. Melamed, J. D. Perkins, A. G. Norman, M. Al-Jassim, E. S. Toberer, and A. C. Tamboli, *J. Mater. Chem. C* **3**, 11017 (2015).
- [21] K. R. Talley, S. R. Bauers, C. L. Melamed, M. C. Papac, K. N. Heinselman, I. Khan, D. M. Roberts, V. Jacobson, A. Mis, G. L. Brennecke *et al.*, *ACS Combinatorial Science* **21**, 537 (2019).
- [22] A. Sharan and S. Lany, *J. Chem. Phys.* **154**, 234706 (2021).
- [23] E. B. Jones and V. Stevanović, *Phys. Rev. B* **96**, 184101 (2017).
- [24] E. B. Jones and V. Stevanović, *npj Comput. Mater.* **6**, 56 (2020).
- [25] A. Zunger, S.-H. Wei, L. G. Ferreira, and J. E. Bernard, *Phys. Rev. Lett.* **65**, 353 (1990).
- [26] A. van de Walle, *CALPHAD* **33**, 266 (2009).
- [27] A. van de Walle, P. Tiwary, M. De Jong, D. Olmsted, M. Asta, A. Dick, D. Shin, Y. Wang, L.-Q. Chen, and Z.-K. Liu, *CALPHAD* **42**, 13 (2013).
- [28] A. Van De Walle, The Alloy-Theoretic Automated Toolkit (ATAT): A User Guide, Brown Engineering.
- [29] P. E. Blöchl, *Phys. Rev. B* **50**, 17953 (1994).
- [30] G. Kresse and D. Joubert, *Phys. Rev. B* **59**, 1758 (1999).
- [31] G. Kresse and J. Hafner, *Phys. Rev. B* **47**, 558 (1993).
- [32] G. Kresse and J. Furthmüller, *Phys. Rev. B* **54**, 11169 (1996).
- [33] J. P. Perdew, K. Burke, and M. Ernzerhof, *Phys. Rev. Lett.* **77**, 3865 (1996).
- [34] S. P. Ong, W. D. Richards, A. Jain, G. Hautier, M. Kocher, S. Cholia, D. Gunter, V. L. Chevrier, K. A. Persson, and G. Ceder, *Comput. Mater. Sci.* **68**, 314 (2013).
- [35] A. Jain, S. P. Ong, G. Hautier, W. Chen, W. D. Richards, S. Dacek, S. Cholia, D. Gunter, D. Skinner, G. Ceder *et al.*, *APL Mater.* **1**, 011002 (2013).
- [36] V. Stevanović, S. Lany, X. Zhang, and A. Zunger, *Phys. Rev. B* **85**, 115104 (2012).
- [37] J. Sun, A. Ruzsinszky, and J. P. Perdew, *Phys. Rev. Lett.* **115**, 036402 (2015).
- [38] J. H. Yang, D. A. Kitchaev, and G. Ceder, *Phys. Rev. B* **100**, 035132 (2019).
- [39] The Materials Project, *Materials Data on ZrZnN2 by Materials Project*, United States (2017), doi:10.17188/1337299.
- [40] S. M. Woodley and R. Catlow, *Nat. Mater.* **7**, 937 (2008).
- [41] G. Hautier, C. Fischer, V. Ehrlicher, A. Jain, and G. Ceder, *Inorg. Chem.* **50**, 656 (2011).
- [42] C. J. Pickard and R. Needs, *J. Phys.: Condens. Matter* **23**, 053201 (2011).
- [43] A. R. Oganov, A. O. Lyakhov, and M. Valle, *Acc. Chem. Res.* **44**, 227 (2011).
- [44] S. Lany, *Phys. Rev. B* **87**, 085112 () (2013).
- [45] S. Lany, *J. Phys.: Condens. Matter* **27**, 283203 () (2015).
- [46] S. Limpijumnong and W. R. L. Lambrecht, *Phys. Rev. B* **63**, 104103 (2001).
- [47] P. Borlido, T. Aull, A. W. Huran, F. Tran, M. A. Marques, and S. Botti, *J. Chem. Theory Comput.* **15**, 5069 (2019).
- [48] M. L. Green, I. Takeuchi, and J. R. Hattrick-Simpers, *J. Appl. Phys.* **113**, 231101 (2013).
- [49] Q.-X. Guo, W.-K. Kwan, X.-L. Cheng, and H. Zhang, *Phys. Status Solidi B* **247**, 67 (2010).

- [50] P. Klumdong, A. Buranawong, S. Chaiyakun, and P. Limsuwan, *Procedia Eng.* **32**, 916 (2012).
- [51] S. Yu, Q. Zeng, A. R. Oganov, G. Frapper, B. Huang, H. Niu, and L. Zhang, *RSC Adv.* **7**, 4697 (2017).
- [52] S. Clarke, C. Michie, and M. Rosseinsky, *J. Solid State Chem.* **146**, 399 (1999).
- [53] S. R. Bauers, D. M. Hamann, A. Patterson, J. D. Perkins, K. R. Talley, and A. Zakutayev, *Jpn. J. Appl. Phys.* **58**, SC1015 (2019).
- [54] D. Partin, D. Williams, and M. O’Keeffe, *J. Solid State Chem.* **132**, 56 (1997).
- [55] S. Siol, A. Holder, J. Steffes, L. T. Schelhas, K. H. Stone, L. Garten, J. D. Perkins, P. A. Parilla, M. F. Toney, B. D. Huey *et al.*, *Sci. Adv.* **4**, eaaq1442 (2018).
- [56] R. Woods-Robinson, Y. Han, J. S. Mangum, C. L. Melamed, B. P. Gorman, A. Mehta, K. A. Persson, and A. Zakutayev, *Matter* **1**, 862 (2019).
- [57] E. Arca, S. Lany, J. D. Perkins, C. Bartel, J. Mangum, W. Sun, A. Holder, G. Ceder, B. Gorman, G. Teeter *et al.*, *J. Am. Chem. Soc.* **140**, 4293 (2018).
- [58] E. Arca, J. D. Perkins, S. Lany, A. Mis, B.-R. Chen, P. Dippo, J. L. Partridge, W. Sun, A. Holder, A. C. Tamboli *et al.*, *Mater. Horiz.* **6**, 1669 (2019).
- [59] K. N. Heinselman, S. Lany, J. D. Perkins, K. R. Talley, and A. Zakutayev, *Chem. Mater.* **31**, 8717 (2019).
- [60] P. F. Ndione, Y. Shi, V. Stevanovic, S. Lany, A. Zakutayev, P. A. Parilla, J. D. Perkins, J. J. Berry, D. S. Ginley, and M. F. Toney, *Adv. Funct. Mater.* **24**, 610 (2014).
- [61] J. J. Cordell, J. Pan, A. C. Tamboli, G. J. Tucker, and S. Lany, *Phys. Rev. Mater.* **5**, 024604 (2021).
- [62] C. M. Caskey, R. M. Richards, D. S. Ginley, and A. Zakutayev, *Mater. Horiz.* **1**, 424 (2014).
- [63] C. M. Rost, E. Sachet, T. Borman, A. Moballegh, E. C. Dickey, D. Hou, J. L. Jones, S. Curtarolo, and J.-P. Maria, *Nat. Commun.* **6**, 8485 (2015).
- [64] A. N. Fioretti, J. Pan, B. R. Ortiz, C. L. Melamed, P. C. Dippo, L. T. Schelhas, J. D. Perkins, D. Kuciauskas, S. Lany, A. Zakutayev *et al.*, *Mater. Horiz.* **5**, 823 (2018).
- [65] S. Lany, A. N. Fioretti, P. P. Zawadzki, L. T. Schelhas, E. S. Toberer, A. Zakutayev, and A. C. Tamboli, *Phys. Rev. Materials* **1**, 035401 (2017).
- [66] A. Togo and I. Tanaka, *Scr. Mater.* **108**, 1 (2015).
- [67] P. C. Quayle, E. W. Blanton, A. Punya, G. T. Junno, K. He, L. Han, H. Zhao, J. Shan, W. R. L. Lambrecht, and K. Kash, *Phys. Rev. B* **91**, 205207 (2015).
- [68] R. R. Schnepf, J. J. Cordell, M. B. Tellekamp, C. L. Melamed, A. L. Greenaway, A. Mis, G. L. Brennecke, S. Christensen, G. J. Tucker, E. S. Toberer *et al.*, *ACS Energy Lett.* **5**, 2027 (2020).
- [69] J. Pan, J. J. Cordell, G. J. Tucker, A. Zakutayev, A. C. Tamboli, and S. Lany, *npj Comput. Mater.* **6**, 63 (2020).
- [70] A. Manzoor, S. Pandey, D. Chakraborty, S. R. Phillpot, and D. S. Aidhy, *npj Comput. Mater.* **4**, 47 (2018).
- [71] H. Ling, S. S. Dwaraknath, and K. A. Persson, *Chem. Mater.* **32**, 2836 (2020).
- [72] C. E. Dreyer, A. Janotti, C. G. Van de Walle, and D. Vanderbilt, *Phys. Rev. X* **6**, 021038 (2016).
- [73] S. Fichtner, N. Wolff, F. Lofink, L. Kienle, and B. Wagner, *J. Appl. Phys.* **125**, 114103 (2019).
- [74] D. Hicks, C. Toher, D. C. Ford, F. Rose, C. De Santo, O. Levy, M. J. Mehl, and S. Curtarolo, *npj Comput. Mater.* **7**, 30 (2021).
- [75] X. Gonze and C. Lee, *Phys. Rev. B* **55**, 10355 (1997).
- [76] A. Zakutayev, N. Wunder, M. Schwarting, J. D. Perkins, R. White, K. Munch, W. Tumas, and C. Phillips, *Sci. Data* **5**, 180053 (2018).